

Supporting Information

Hollow cobalt phosphate microspheres for sustainable electrochemical ammonia production through rechargeable Zn-N₂ battery

Jin-Tao Ren ^a, Lei Chen ^a, Yuping Liu ^b and Zhong-Yong Yuan ^{a,b,*}

^a *National Institute for Advanced Materials, School of Materials Science and Engineering, Nankai University, Tianjin 300350, China.*

^b *Key Laboratory of Advanced Energy Materials Chemistry (Ministry of Education), Collaborative Innovation Center of Chemical Science and Engineering (Tianjin), Nankai University, Tianjin 300071, China.*

*Corresponding author. *E-mail:* zyyuan@nankai.edu.cn

1. Experimental Section

1.1. Preparation of electrocatalysts

In a typical synthesis, 3 mmol cobalt nitrate, 0.4 mmol bis(hexamethylene triamine penta (methylene phosphonic acid)) (BHMTMPMA), and 6 mmol urea were dissolved into the mixture of ethanol and deionized water with the volume ratio of 1:3. Then the obtained solution was transferred into the Teflon-lined autoclave and kept at 140 °C for 24 h. The precipitates were washed with deionized water and dried at 80 °C, which was named as Co-BPA. The prepared Co-BPA was then treated at 900 °C for 2 h in flowing N₂, and the obtained material was named as CoPi/HSNPC.

For the comparison, the cobalt phosphonates with featureless structure were also prepared. Typically, 3 mmol cobalt nitrate, 0.4 mmol BHMTMPMA were added into deionized water with stirring, and the final pH was adjusted by ammonium hydroxide to about 5. The obtained mixture was transferred into a Teflon-lined autoclave and heated at 140 °C for 24 h. The synthesized products were filtered, washed, dried, and pyrolyzed at 900 °C for 2 h in N₂ atmosphere, and the resultant material was denoted as CoPi/NPC.

To discuss the effect of carbon substrates in CoPi/HSNPC on electrochemical performance, a N,P-dual-doped carbon matrix obtained from the direct pyrolysis of BHMTMPMA at 900 °C for 2 h in N₂ atmosphere was also fabricated, which was named as NPC.

To investigate the positive effect of phosphate groups on electrochemical reactions, the cobalt oxides were also prepared through hydrothermal treatment process. Typically, 1.2 mmol cobalt nitrate was dissolved in 6 mL ethanol, 75 mmol NaOH was dissolved in 7.5 mL ethanol. Then the former solution was slowly dropped into the latter solution under magnetic stirring, and the resulting solution and 0.3 g hexadecyl trimethyl ammonium bromide (CTAB) were together transferred into a Teflon-lined autoclave at 180 °C for 5 h. The resulting product was collected and washed with ethanol for several times and dried at 80 °C, which was labeled as CoO NPs.

1.2. Materials characterization

Scanning electron microscopy (SEM) and transition electron microscopy (TEM) were carried out on the Jeol JSM-7800F and Jeol JEM-2800 instruments, respectively. X-ray diffraction (XRD) patterns were measured on a Bruker D8 Focus diffractometer with Cu K α radiation. Raman spectra were measured on a Thermo-Fisher Scientific DXR spectrometer. Fourier transform infrared (FT-IR) spectra were obtained on a Bruker VECTOR 22 spectrometer with the KBr pellet technique. X-ray photoelectron spectroscopy (XPS) measurements were performed on a Thermo Scientific ESCALAB 250Xi spectrometer equipped with a monochromatic Al K α X-ray source (1486.6 eV). Thermogravimetry analysis (TGA) was performed using a TA SDT Q600 instrument. The Brunauer–Emmett–Teller (BET) specific surface area was obtained by N₂ adsorption–desorption analysis on a Quantachrome Nova 2000e sorption analyzer at liquid temperature. The UV–vis absorbance spectroscopy was measured on a UV–vis spectrophotometer (Kenfan KU-T1810). The *in-situ* FTIR spectroscopic data of

electrocatalytic reaction were collected on the electrochemical *in-situ* Fourier transform infrared spectroscope (Nicolet Nexus 870). The ^1H NMR (nuclear magnetic resonance) spectra were obtained using superconducting Fourier transform nuclear magnetic resonance spectrometer (Bruker Avance-600).

1.3. Electrochemical measurements

The NRR performance tests were carried out on the CHI 760E electrochemical station using a three-electrode system with an H-type cell and Nafion 117 membrane as separator. Before NRR electrolysis, the Nafion membrane was first squeezed in ultrapure water at 80 °C for 1 h, followed by immersion in H_2O_2 (5%) solution at 80 °C for another 1 h. Then, the membrane was protonated in 0.5 M H_2SO_4 at 80 °C for 1 h and finally washed by ultrapure water for 2 h. The Ag/AgCl and Pt wire were used as the reference and counter electrodes, respectively, and the catalyst film coated carbon paper was employed as the working electrode. To prepare the working electrode, typically, 5 mg catalysts and 20 μL Nafion (5 wt%) were added into the mixture of isopropanol and deionized water ($v:v = 3:1$) followed by sonication. Subsequently, certain amount of the homogeneous catalyst ink was drop-coated onto the clean carbon paper, dried in air to prepare the working electrode. The measured potential (vs. Ag/AgCl) in this work was normalized to reversible hydrogen electrode (vs. RHE) according to Nernst equation.

Prior to NRR measurement, all samples were immersed into and washed with 0.1 M KOH solution three times to exclude any NH_3 or NH_4^+ contaminant. The high-pure N_2 gas and Ar gas were purified by flowing them through 0.1 M KOH solution to remove any N contamination in the flowing gases before entering the electrolyte. Before data collection, the electrolyte was pre-saturated with high-purity N_2 for 30 min, and the working electrode were activated by steady-state potential sweeping cycles in the range of 0.15 to -0.65 V (vs. RHE) at $50 \text{ mV}\cdot\text{s}^{-1}$ in an N_2 -saturated 0.1 M KOH solution for 20 cycles. For NRR tests, a potentiostatic test was conducted for 2 h in an N_2 -saturated 0.1 M KOH solution under atmospheric pressure and constant temperature. High-pure N_2 was continuously purged in the cathode compartment under a constant flow rate. Corresponding tests in an Ar-saturated 0.1 M KOH solution were also conducted as control experiments. Linear sweep voltammetry (LSV) was performed at $2 \text{ mV}\cdot\text{s}^{-1}$ in a 0.1 M KOH solution between 0.1 and -0.5 V (vs. RHE). All polarization curves were obtained without current resistance (iR) compensation.

For OER measurement, the anodic linear sweep voltammetry (LSV) was collected in O_2 -saturated 1.0 M KOH with the scan rate of 2 mV s^{-1} . All polarization curves were presented with current resistance (iR) compensation.

Zn- N_2 battery test, the rechargeable Zn- N_2 battery experiment was measured with home-made Zn- N_2 configuration with H-cell arrangement separated by the Nafion 117 membrane to avoid destroying anodic or cathodic products. The prepared samples were directly used as cathodic electrode, and the Zn plate was used as the anodic electrode. Both electrodes were immersed into 1.0 M KOH, and the catholyte was bubbled with N_2

continuously. The cycling measurements was carried out for 4 h per cycle (2 h discharge and 2 h charge) under certain current density. After each discharging process during cycling test, the catholyte was replaced by the fresh KOH electrolyte to extract N₂ reduction products.

1.4. Detection of ammonia and hydrazine

The concentration of produced ammonia was determined by the indophenol blue method using UV-Vis spectrophotometry. Prior to detection of ammonia, several reagent were prepared. Chromogenic reagent A: 5 wt% salicylic acid and 5 wt% sodium citrate were added into 1 M NaOH. Oxidizing solution B: 0.05 M sodium hypochlorite. Catalyzing reagent C: 1 wt% sodium nitroferricyanide. In detail, 2 mL of standard solutions or sample solutions from the post-electrolysis electrolyte were mixed with 2 mL of chromogenic reagent A, 1 mL of oxidizing solution B and then with 0.2 mL of catalyzing reagent C. After shaking and standing for 2 h, the absorption spectrum of the resulting solution was measured using a UV-Vis spectrophotometer in the wavelength range 500 to 800 nm. And the absorbance at the wavelength of 656 nm was recorded. And the background was corrected with a blank solution. The standard curve was calibrated using standard NH₄Cl solution with a series of concentrations in 0.1 KOH.

The probable byproduct N₂H₄ in the cathode compartment during the NRR reaction was also estimated using the Watt and Chrisp method. The color reagent was prepared by mixing of HCl (37 wt%, 30 mL), ethanol (300 mL), and para-(dimethylamino) benzaldehyde (5.99 g). The 2 mL of above prepared color reagent was added into 2 mL aliquot of the reaction solution at room temperature. The absorbance of the resulting solution was measured at 455 nm.

1.5. Calculation of ammonia yield rate and Faradaic efficiency

The yield rate of NH₃ (v_{NH_3}) was calculated using the following equation:

$$v_{\text{NH}_3} = (C_{\text{NH}_3} \times V) / (t \times m_{\text{cat}})$$

The Faradaic efficiency (FE) for NRR was defined as the proportion of the electric charges used for synthesizing NH₃ among the total charges passing through the electrodes during NRR electrolysis. Assuming three electrons were needed to produce one NH₃ molecule, the FE could be calculated as follows:

$$\text{FE} = (3F \times C_{\text{NH}_3} \times V) / 17 \times Q$$

where C_{NH_3} is the ammonia concentration measured by the indophenol method ($\mu\text{g mL}^{-1}$); V (mL) is the volume of the reaction electrolyte after NRR; t is the electro-reduction reaction time (h); m_{cat} is the effective weight of the catalyst on the working electrode (mg). F is the Faraday constant; Q is the quantity of applied electricity.

2. Supplementary Figures

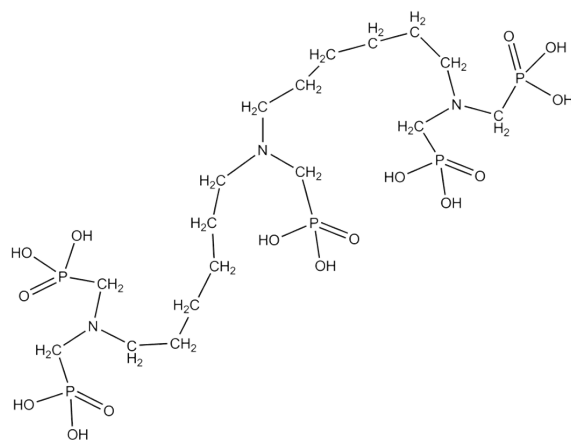


Fig. S1 Molecule structure of BHMTMPMPA.

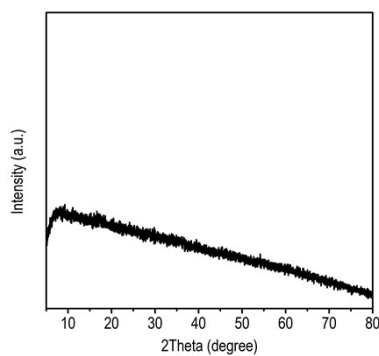


Fig. S2 XRD pattern of as-prepared Co-BPA.

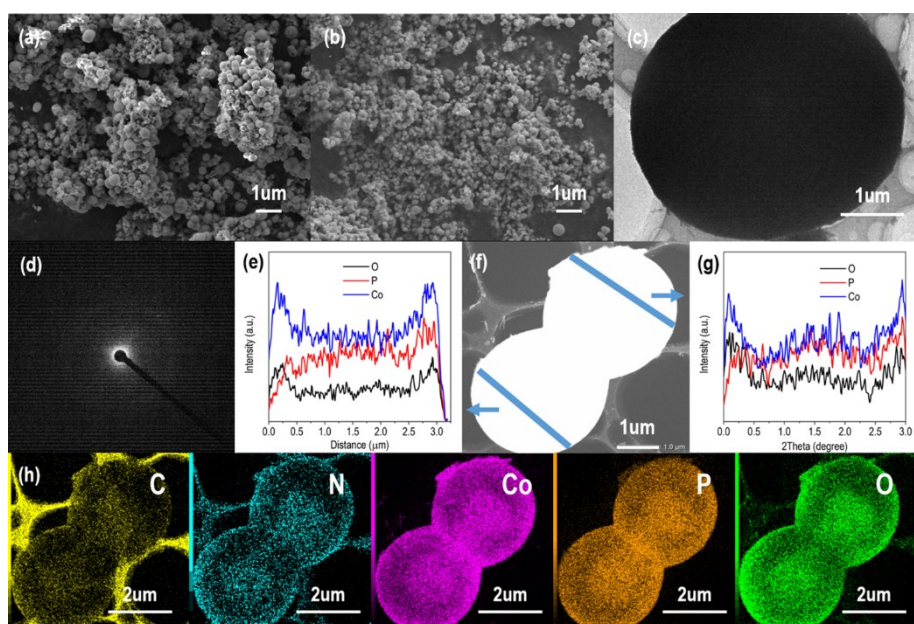


Fig. S3 (a, b) SEM and (c) TEM images and (d) SAED pattern of Co-BPA. (e-g) STEM image and corresponding line-scan TEM-EDS elemental distribution curves of Co-BPA. (h) EDS elemental mapping of Co-BPA.

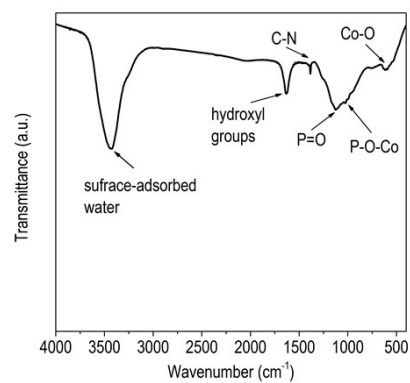


Fig. S4 FT-IR spectrum of CoPi/HSNPC

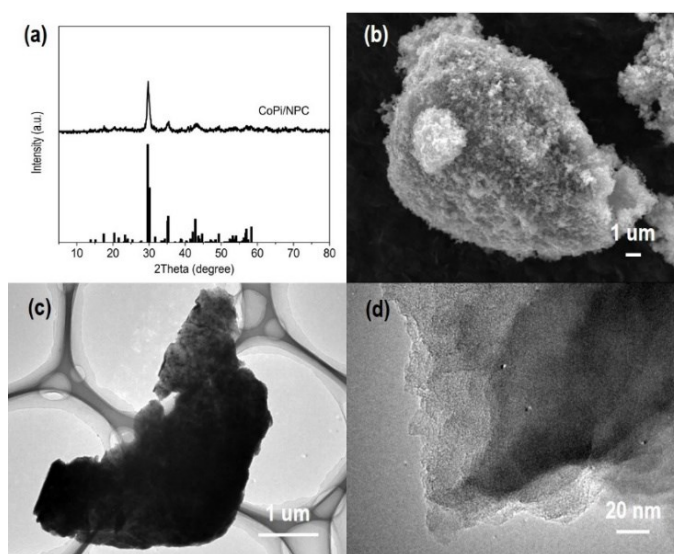


Fig. S5 (a) XRD pattern, (b) SEM and (c, d) TEM images of CoPi/NPC.

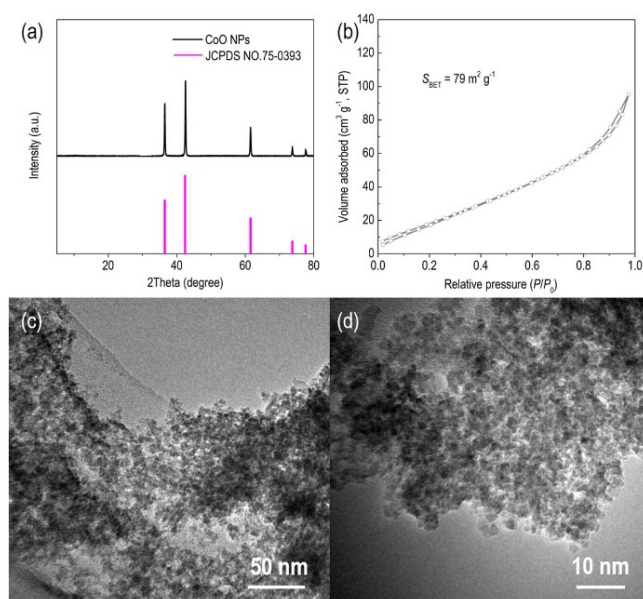


Fig. S6 (a) XRD pattern, (b) N₂ adsorption-desorption isotherms, and (c, d) TEM images of CoO NPs sample.

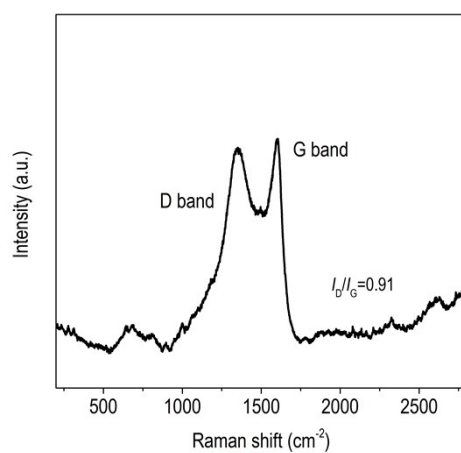


Fig. S7 Raman spectrum of CoPi/HSNPC.

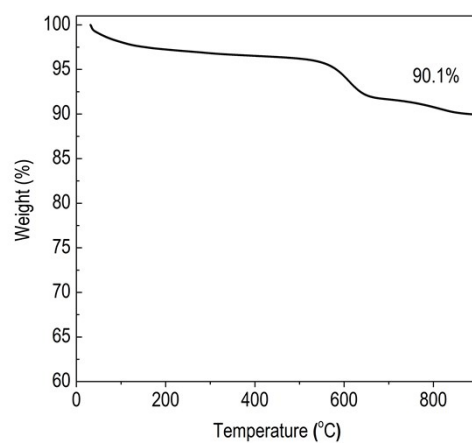


Fig. S8 TGA curves of CoPi/HSNPC measured in flowing air.

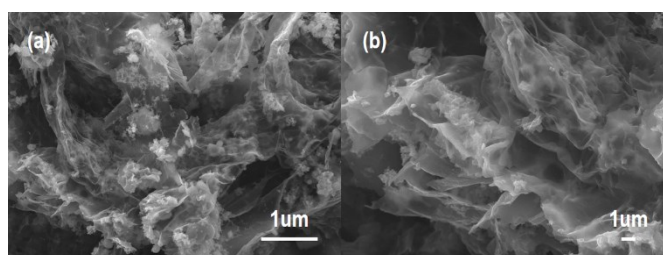


Fig. S9 (a) and (b) SEM images of as-prepared NPC.

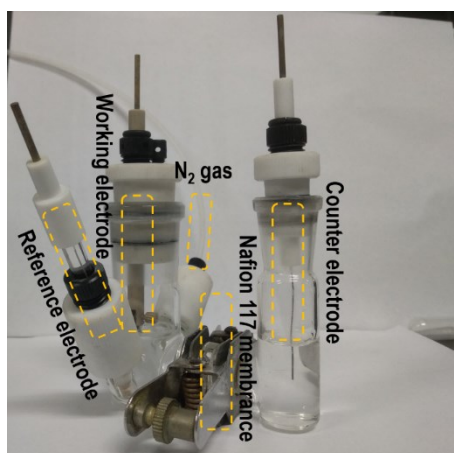


Fig. S10 The three-electrode electrocatalytic system in this work for NRR.

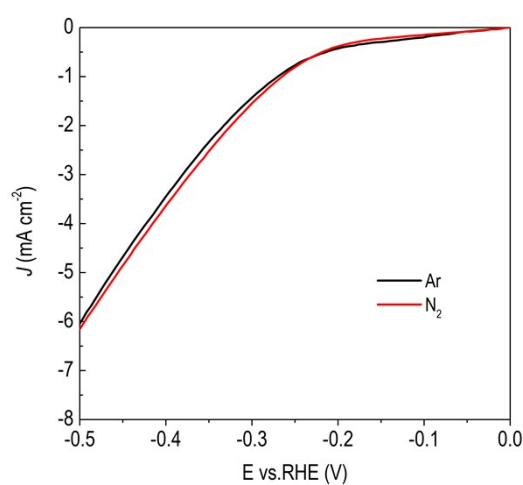


Fig. S11 Polarization curves of CoPi/HSNPC in N_2 - and Ar-saturated 0.1 M KOH.

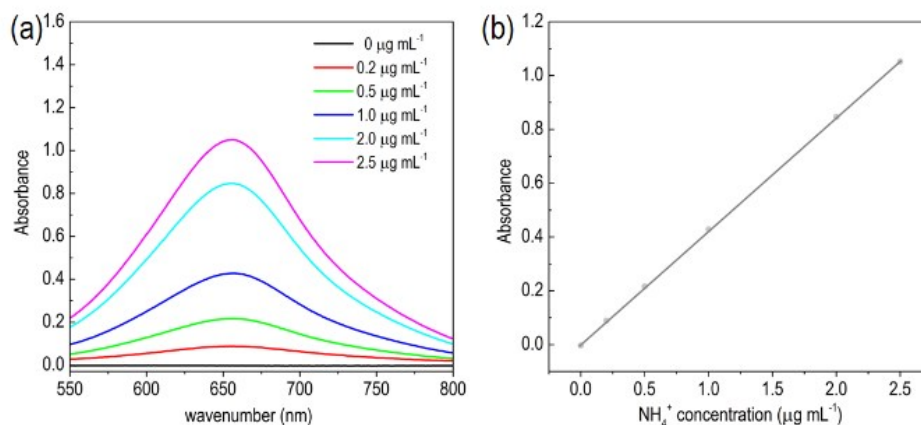


Fig. S12 UV-Vis absorption spectra (a) and calibration curves (b) for NH_4^+ in 0.1 M KOH by indophenol blue method. The standard curve was calibrated using standard NH_4Cl solution with a series of concentrations from 0 to 2.5 μg in 0.1 KOH. The fitted curves obtained a good linear relation of absorbance with NH_4^+ concentration, $y = 0.42082x + 0.00315$, $R^2 = 0.999$.

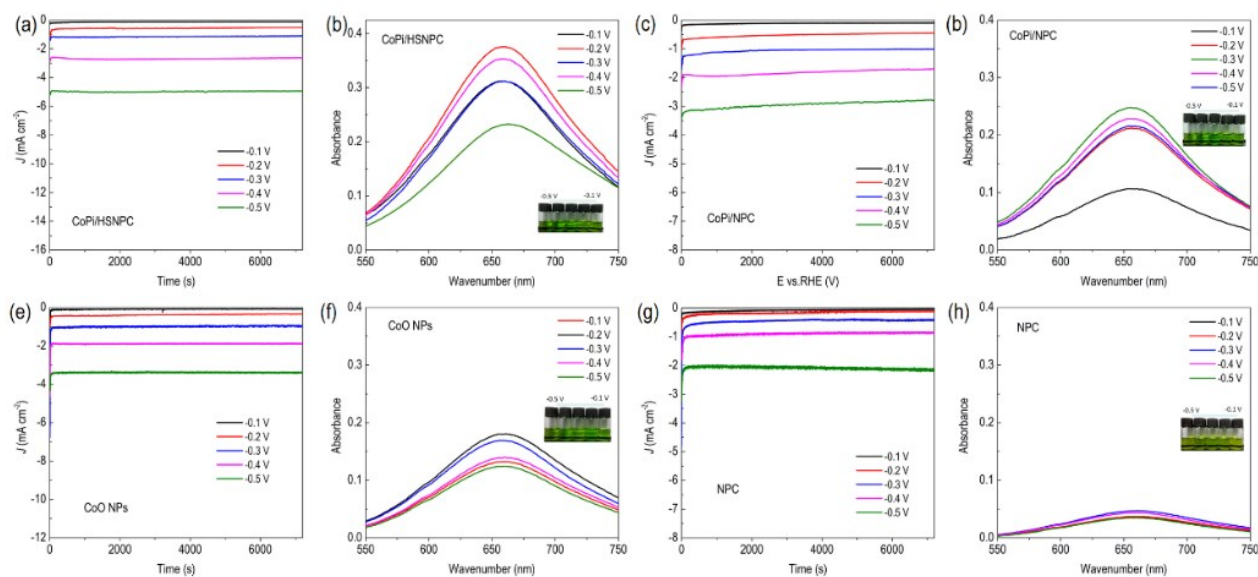


Fig. S13 Chronoamperometry curves and the UV-vis absorption spectra of electrolyte after electrolyzation in N_2 -saturated at varied potentials by indophenol blue method for CoPi/HSNPC (a, b), CoPi/NPC (c, d), CoO NPs (e, f), and NPC (g, h). The inset is the photograph of electrolyte treated using the indophenol blue method.

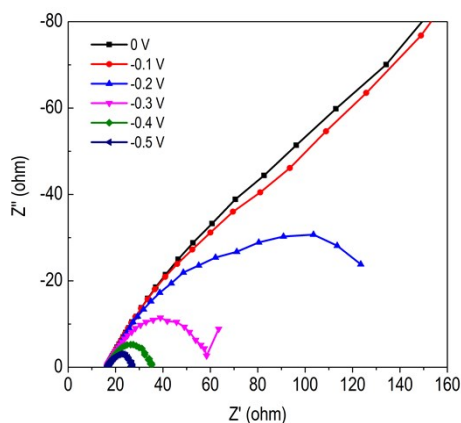


Fig. S14 EIS of CoPi/HSNPC at different cathodic potentials in 0.1 M KOH.

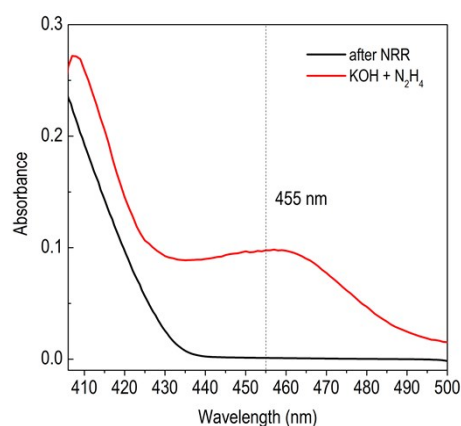


Fig. S15 UV-Vis absorption spectra of the electrolyte after electrolyzation in N_2 -saturated at -0.2 V vs. RHE for CoPi/HSNPC sample and the fresh KOH electrolyte containing N_2H_4 by the Watt-Chrisp method.

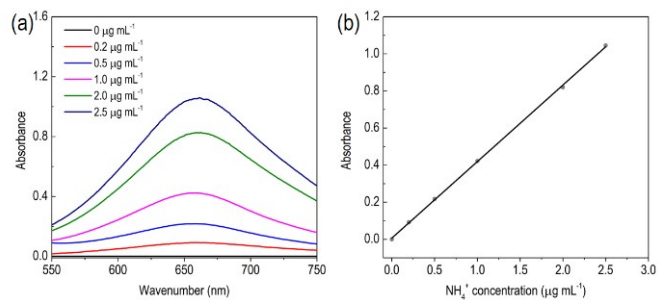


Fig. S16 UV-Vis absorption spectra (a) and calibration curves (b) for NH_4^+ in 1.0 M KOH by indophenol blue method. The fitted curves obtained a good linear relation of absorbance with NH_4^+ concentration, $y = 0.4127x + 0.0063$, $R^2 = 0.999$.

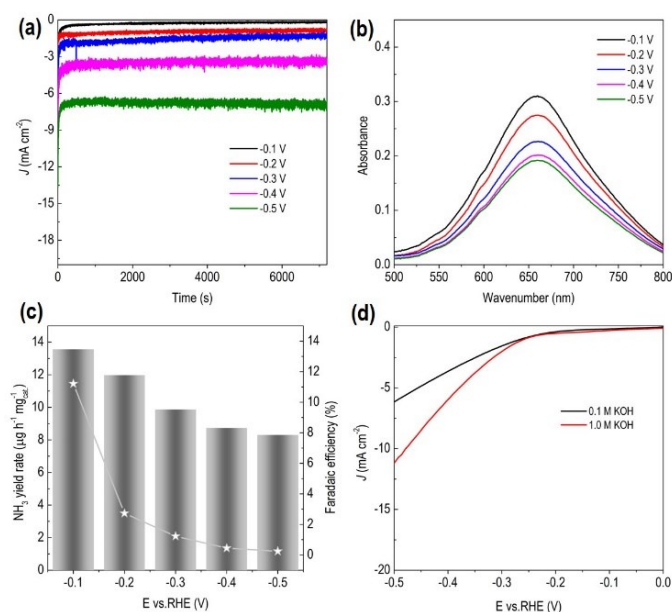


Fig. S17 (a) Chronoamperometry curves and (b) UV-vis absorption spectra of electrolyte after electrolyzation in N_2 -saturated 1.0 M KOH at varied potentials by indophenol blue method for CoPi/HSNPC. (c) NH_3 yield rate and Faradaic efficiency of CoPi/HSNPC at varied potentials in 1.0 M KOH. (d) LSV curves of CoPi/HSNPC in 0.1 M and 1.0 M KOH.

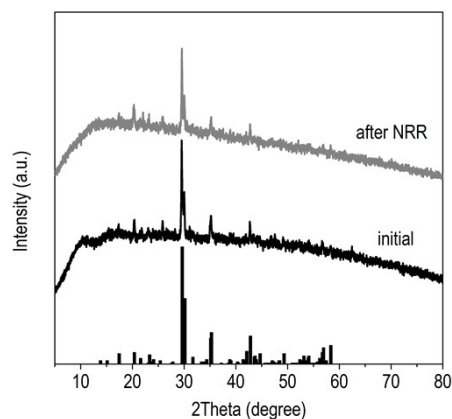


Fig. S18 XRD patterns of CoPi/HSNPC before and after NRR recycling tests.

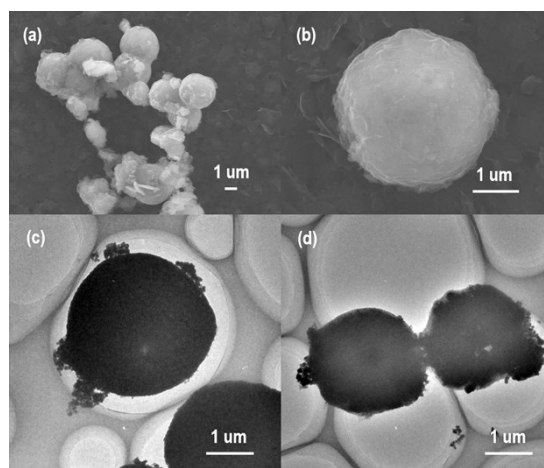


Fig. S19 (a, b) SEM and (c, d) TEM images of CoPi/HSNPC after NRR recycling tests.

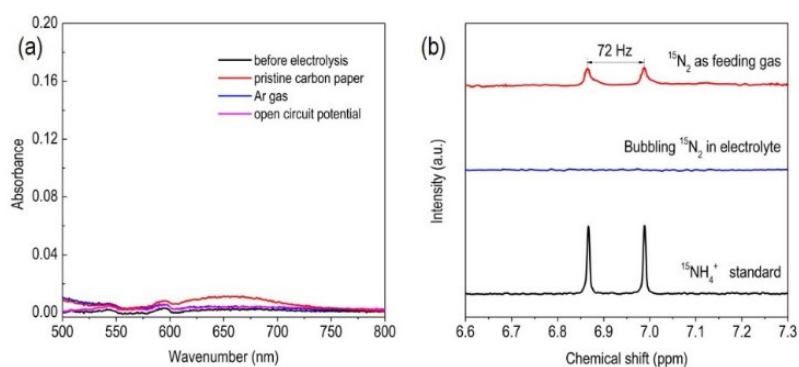


Fig. S20 (a) UV-Vis spectra of the electrolyte stained with indophenol indicator before and after 2 h electrolysis for CoPi/HSNPC at the potential of -0.2 V vs. RHE under different electrochemical conditions. (b) NMR analysis of the reacted solution by feeding $^{15}\text{N}_2$ gas after NRR electrolysis.

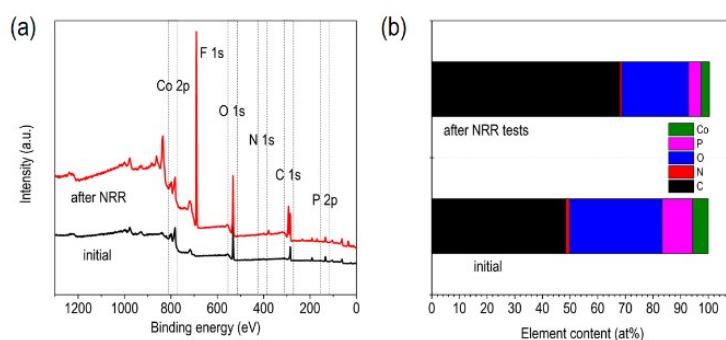


Fig. S21 (a) XPS survey scan and (d) element content of CoPi/HSNPC catalyst before and after NRR tests.

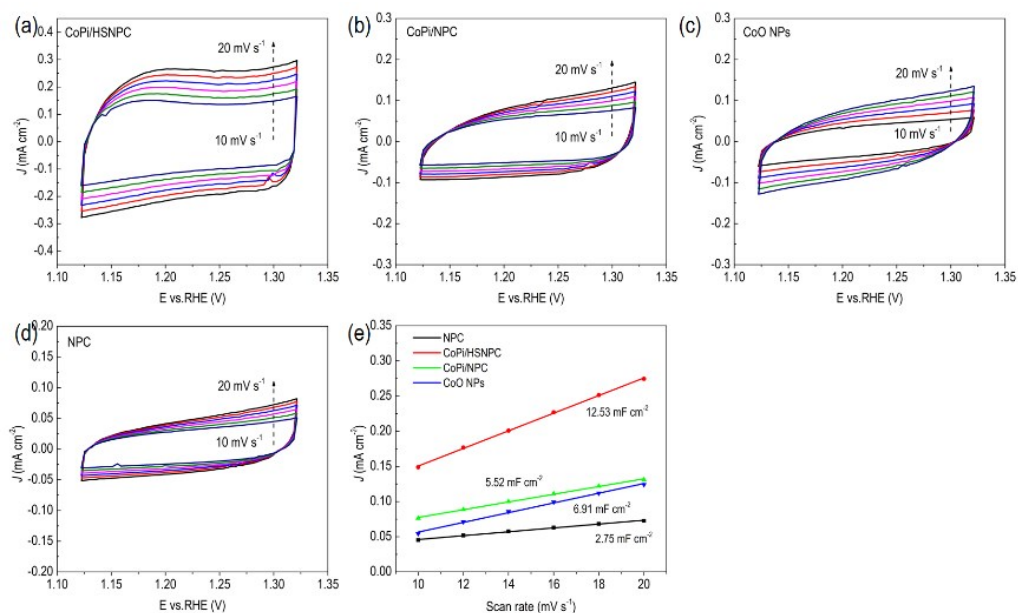


Fig. S22 CV curves of CoPi/HSNPC (a), CoPi/NPC (b), CoO NPs (c), and NPC (d) under the scan rates from 10 to 20 mV s⁻¹. (e) Plots of the current density as a function against the corresponding scan rates of these samples.

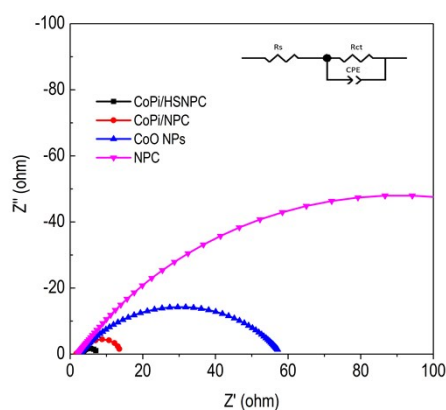


Fig. S23 Nyquist plots of CoPi/HSNPC, CoPi/NPC, CoO NPs, and NPC in 1.0 M KOH. Inset is the corresponding equivalent circuit diagram consisting of an electrolyte resistance (R_s), a charge-transfer resistance (R_{ct}), and a constant-phase element (CPE).

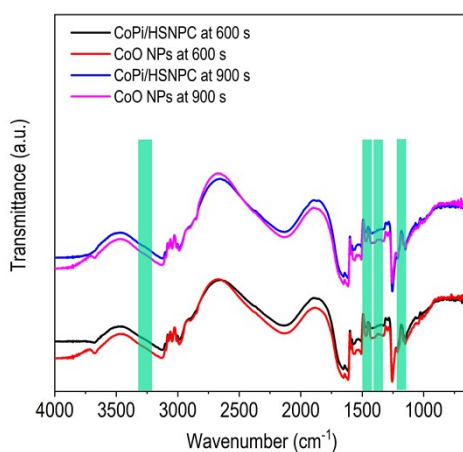


Fig. S24 Electrochemical *in situ*-FTIR spectroscopy of the NRR on CoPi/HSNPC and CoO NPs.

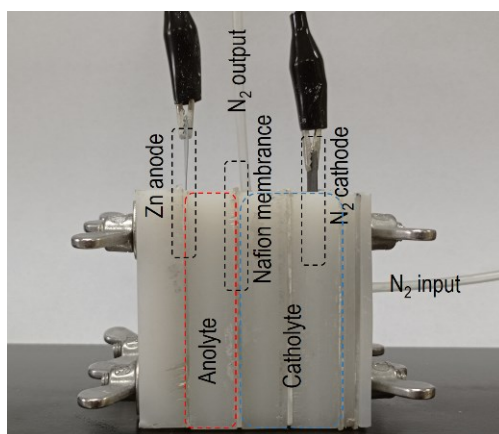


Fig. S25 Typical photograph of this home-made Zn-N₂ battery.

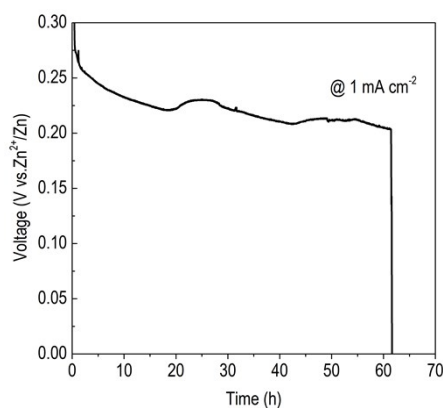


Fig. S26 Galvanostatic discharge curve of CoPi/HSNPC catalyzed Zn-N₂ battery. The energy density (mWh g⁻¹) is calculated according to the equation of (current × service hours × average discharge voltage) / (weight of consumed zinc).

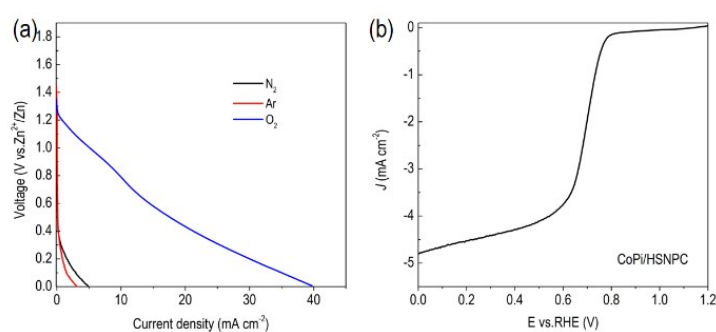


Fig. S27 (a) Discharge polarization curves of CoPi/HSNPC-catalyzed battery with different feeding gas. (b) Oxygen reduction reaction polarization curves of CoPi/HSNPC catalysts measured in 0.1 M O₂-saturated 0.1 M KOH with the rotation speed of 1600 rpm.

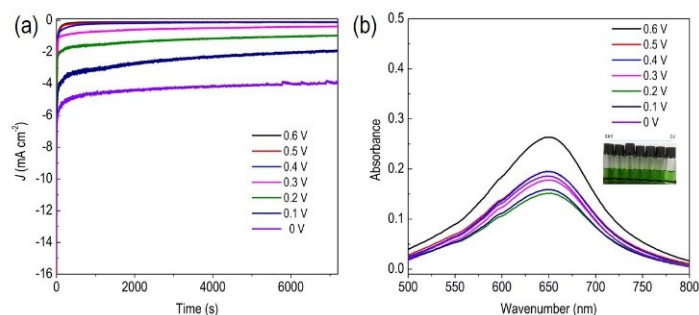


Fig. S28 (a) Galvanostatic discharge curves of CoPi/HSNPC-catalyzed battery under different voltages in N_2 -saturated 1.0 M KOH. (b) UV-vis absorption spectra of electrolyte after electrolyzation in N_2 -saturated at varied voltages for CoPi/HSNPC-catalyzed battery by indophenol blue method.

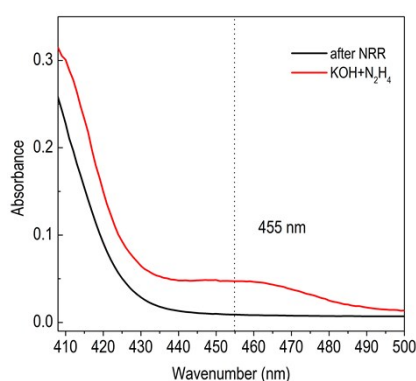


Fig. S29 UV-Vis absorption spectra of electrolyte after electrolyzation in N_2 -saturated at 0.6 V vs. Zn^{2+}/Zn by the Watt-Chrisp method for CoPi/HSNPC-catalyzed battery.

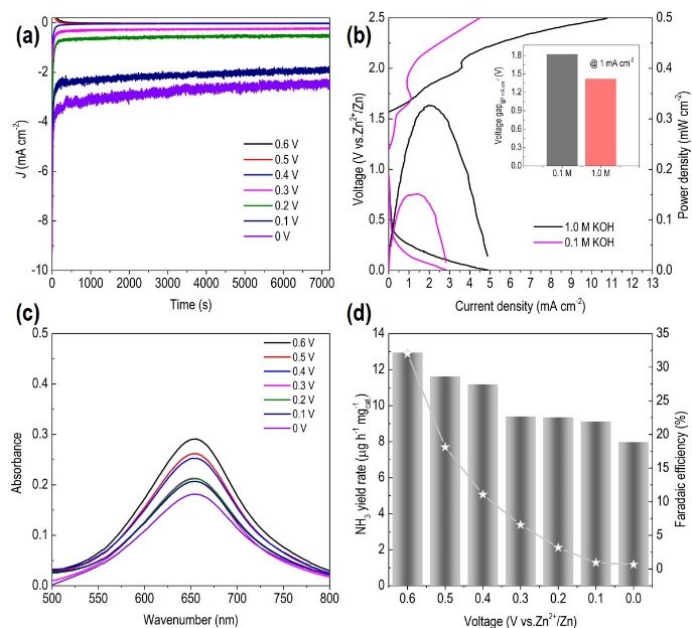


Fig. S30 (a) Galvanostatic discharge curves of CoPi/HSNPC-catalyzed battery under different voltages in N_2 -saturated 0.1 M KOH. (b) Charge-discharge polarization curves and the corresponding power density curves of CoPi/HSNPC-catalyzed battery with different electrolyte. Inset is the voltage gap at the current density of 1.0 mA. (c) UV-vis absorption spectra of electrolyte after electrolyzation in N_2 -saturated at varied voltages for CoPi/HSNPC-catalyzed battery by indophenol blue method. (d) NH_3 yield rate and Faradaic efficiency vs. Voltage (V vs. Zn^{2+}/Zn).

cm⁻². (c) UV–vis absorption spectra of electrolyte after electrolyzation in N₂-saturated at varied voltages for CoPi/HSNPC-catalyzed battery by indophenol blue method. (d) NH₃ yield rate and Faradaic efficiency of CoPi/HSNPC at varied potentials in 0.1 M KOH.

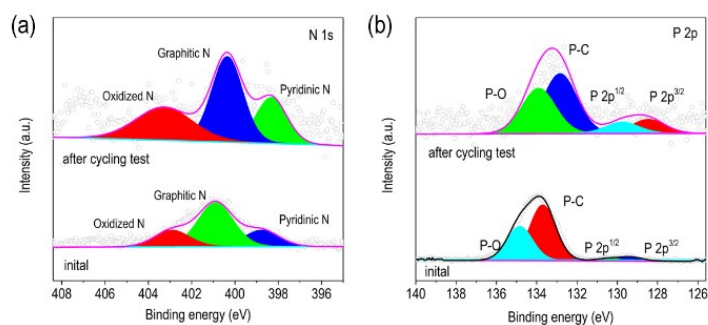


Fig. S31 High-resolution XPS spectra of N 1s (a), and P 2p (b) region of CoPi/HSNPC before and after Zn-N₂ battery cycling tests.

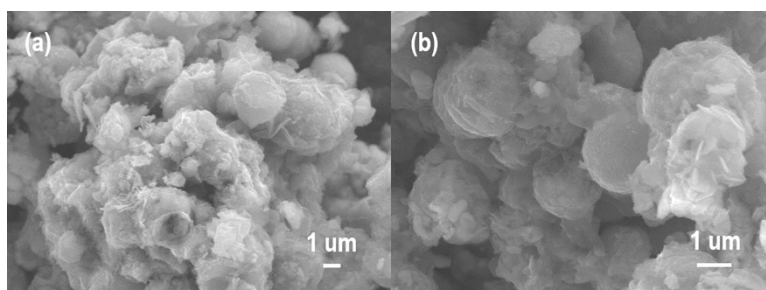


Fig. S32 (a, b) SEM images of CoPi/HSNPC after Zn-N₂ battery cycling tests.

3. Supplementary Tables

Tables S1. Summary of the NRR performance of recent reported Co-based and other nonprecious electrocatalysts in alkaline conditions.

Catalyst	Electrolyte	NH ₃ yield rate	Faradaic efficiency (%)	Potential	Reference
CoPi/HSNPC	0.1 M KOH	16.48 $\mu\text{g h}^{-1} \text{mg}_{\text{cat.}}^{-1}$	4.46	-0.2 V vs. RHE	This work.
CoP hollow nanocage	1.0 M KOH	10.78 $\mu\text{g h}^{-1} \text{mg}_{\text{cat.}}^{-1}$	7.36	-0.4 V vs. RHE	[1]
Fe-N/C-CNTs	0.1 M KOH	34.83 $\mu\text{g h}^{-1} \text{mg}_{\text{cat.}}^{-1}$	9.28	-0.2 V vs. RHE	[2]
Pd_{0.2}Cu_{0.8}/rGO	0.1 M KOH	2.8 $\mu\text{g h}^{-1} \text{mg}_{\text{cat.}}^{-1}$	~4.5	-0.2 V vs. RHE	[3]
B/N-CNF	0.1 M KOH	20.0 $\mu\text{g h}^{-1} \text{mg}_{\text{cat.}}^{-1}$	13.2	-0.5 V vs. RHE	[4]
γ-Fe₂O₃ nanoparticles-CNT	0.1 M KOH	0.2 $\mu\text{g h}^{-1} \text{mg}_{\text{cat.}}^{-1}$	1.9	-1.0 V vs. Ag/AgCl	[5]
ZIF-derived carbon	0.1 M KOH	57.8 $\mu\text{g h}^{-1} \text{cm}^{-2}$	10.2	-0.3 V vs. RHE	[6]
W₂N₃	0.1 M KOH	11.7 $\mu\text{g h}^{-1} \text{mg}_{\text{cat.}}^{-1}$	11.7	-0.2 V vs. RHE	[7]
Eex-COF/NC	0.1 M KOH	12.5 $\mu\text{g h}^{-1} \text{mg}_{\text{cat.}}^{-1}$	45.4	-0.2 V vs. RHE	[8]
Fe-N/C-CNTs	0.1 M KOH	34.8 $\mu\text{g h}^{-1} \text{mg}_{\text{cat.}}^{-1}$	9.3	-0.2 V vs. RHE	[9]
Fe₂O₃/CNT	0.5 M KOH	0.26 $\mu\text{g h}^{-1} \text{mg}_{\text{cat.}}^{-1}$	0.164	-2.0 V vs. Ag/AgCl	[10]
Single-atom-Mo/N-doped porous carbon	0.1 M KOH	34.0 $\mu\text{g h}^{-1} \text{mg}_{\text{cat.}}^{-1}$	14.6	-0.3 V vs. RHE	[11]
Zr-doped TiO₂	0.1 M KOH	8.9 $\mu\text{g h}^{-1} \text{cm}^{-2}$	17.3	-0.45 V vs. RHE	[12]
Co₃Fe-MOF	0.1 M KOH	8.79 $\mu\text{g h}^{-1} \text{mg}_{\text{cat.}}^{-1}$	25.64	-0.2 V vs. RHE	[13]
FeS@MoS₂/CFC	0.1 M KOH	2.46 $\mu\text{g h}^{-1} \text{mg}_{\text{cat.}}^{-1}$	0.067	-0.5 V vs RHE	[14]
Fe_{SA}-N-C	0.1 M KOH	7.48 $\mu\text{g h}^{-1} \text{mg}_{\text{cat.}}^{-1}$	56.55	0 V vs. RHE	[15]
K₂Ti₄O₉ nanobelt	0.1 M KOH	22.8 $\mu\text{g h}^{-1} \text{mg}_{\text{cat.}}^{-1}$	5.9	-0.5 V vs. RHE	[16]
PdO/Pd/CNTs	0.1 M NaOH	18.2 $\mu\text{g h}^{-1} \text{mg}_{\text{cat.}}^{-1}$	11.5	0.1 V vs. RHE	[17]
Pd-Co/CuO	0.1 M KOH	10.0 $\mu\text{g h}^{-1} \text{mg}_{\text{cat.}}^{-1}$	2.2	-0.2 V vs. RHE	[18]
Rh nanosheet	0.1 M KOH	23.88 $\mu\text{g h}^{-1} \text{mg}_{\text{cat.}}^{-1}$	0.2	-0.2 V vs. RHE	[19]

Table S2. The comparison of OER performance of as-prepared CoPi/HSNPC and some active nonprecious OER electrocatalysts.

Catalyst	Electrolyte	Overpotential (mV) @ 10 mA cm ⁻²	Tafel slope (mV dev ⁻¹)	Reference
CoPi/HSNPC	1.0 M KOH	341	82	This work.
CoO _x -4h nanoplates	1.0 M KOH	306	67	[20]
Co _{3-x} O ₄	1.0 M KOH	268	38.2	[21]
Fe1Co1-ONS	0.1 M KOH	308	36.8	[22]
CoO/C-500	1.0 M KOH	200	59.5	[23]
Co ₂ (OH) ₂ BDC nanosheets	1.0 M KOH	263	74	[24]
Fe-incorporated Co _x S _y	1.0 M KOH	304	54.2	[25]
CoO-L	1.0 M KOH	369	46	[26]
CoFe ₂ O ₄ nanorods	1.0 M KOH	355	96	[27]
Hierarchical Mn-Co phosphide yolk-shell spheres	1.0 M KOH	330	59	[28]
Zn-CoSe ₂ NAs	1.0 M KOH	286	37	[29]
Fe-CoP/CoO	1.0 M KOH	219	52	[30]
Co ₃ O ₄ /CoO	1.0 M KOH	302	68.6	[31]
CoO _x (Ce)	1.0 M KOH	229	63.7	[32]
NiMoP@CoCH/CC	1.0 M KOH	267 @40 mA cm ⁻²	99	[33]
Fe-CoO	1.0 M KOH	304	38	[34]
Co@NPC-H	1.0 M KOH	350	57	[35]

Tables S3. Summary of the NRR performance of recent reported Zn-N₂ battery.

Catalyst	Electrolyte	Peak power density	Voltage (V vs Zn ²⁺ /Zn) @ highest NH ₃ yield rate	NH ₃ yield rate	Faradaic efficiency	Reference
CoPi/HSNPC	1.0 M KOH	0.33 mW cm ⁻²	0.6	11.58	24.39%	This work.
nano-Cu	0.1 M KOH	10.1 μW cm ⁻²	~0.925	~0.125 μg h ⁻¹ cm ⁻²	~59%	[36]
exfoliated NbS ₂ nanosheets	N.A.	0.31 mW cm ⁻²	N.A.	N.A.	N.A.	[37]
VN@NSC-900	0.1 M KOH	16.42 μW cm ⁻²	~0.525	0.172 μg h ⁻¹ cm ⁻²	~12%	[38]

4. Supplementary References

- [1] W. Guo, Z. Liang, J. Zhao, B. Zhu, K. Cai, R. Zou, Q. Xu, Hierarchical Cobalt Phosphide Hollow Nanocages toward Electrocatalytic Ammonia Synthesis under Ambient Pressure and Room Temperature, *Small Methods* 2 (2018) 1800204.
- [2] Y. Wang, X. Cui, J. Zhao, G. Jia, L. Gu, Q. Zhang, L. Meng, Z. Shi, L. Zheng, C. Wang, Z. Zhang, W. Zheng, Rational Design of Fe–N/C Hybrid for Enhanced Nitrogen Reduction Electrocatalysis under Ambient Conditions in Aqueous Solution, *ACS Catal.* 9 (2019) 336-344.
- [3] M.M. Shi, D. Bao, S.J. Li, B.R. Wulan, J.M. Yan, Q. Jiang, Anchoring PdCu amorphous nanocluster on graphene for electrochemical reduction of N_2 to NH_3 under ambient conditions in aqueous solution, *Adv. Energy Mater.* 8 (2018) 1800124.
- [4] Y. Kong, Y. Li, B. Yang, Z. Li, Y. Yao, J. Lu, L. Lei, Z. Wen, M. Shao, Y. Hou, Boron and nitrogen co-doped porous carbon nanofibers as metal-free electrocatalysts for highly efficient ammonia electrosynthesis, *J. Mater. Chem. A* 7 (2019) 26272-26278.
- [5] S. Chen, S. Perathoner, C. Ampelli, C. Mebrahtu, D. Su, G. Centi, Electrocatalytic synthesis of ammonia at room temperature and atmospheric pressure from water and nitrogen on a carbon - nanotube - based electrocatalyst, *Angew. Chem. Int. Ed.* 56 (2017) 2699-2703.
- [6] S. Mukherjee, D.A. Cullen, S. Karakalos, K. Liu, H. Zhang, S. Zhao, H. Xu, K.L. More, G. Wang, G. Wu, Metal-organic framework-derived nitrogen-doped highly disordered carbon for electrochemical ammonia synthesis using N_2 and H_2O in alkaline electrolytes, *Nano Energy* 48 (2018) 217-226.
- [7] H. Jin, L. Li, X. Liu, C. Tang, W. Xu, S. Chen, L. Song, Y. Zheng, S.Z. Qiao, Nitrogen vacancies on 2D layered W_2N_3 : A stable and efficient active site for nitrogen reduction reaction, *Adv. Mater.* 31 (2019) 1902709.
- [8] S. Liu, M. Wang, T. Qian, H. Ji, J. Liu, C. Yan, Facilitating nitrogen accessibility to boron-rich covalent organic frameworks via electrochemical excitation for efficient nitrogen fixation, *Nat. Commun.* 10 (2019) 3898.
- [9] H. Cheng, L.X. Ding, G.F. Chen, L. Zhang, J. Xue, H. Wang, Molybdenum Carbide Nanodots Enable Efficient Electrocatalytic Nitrogen Fixation under Ambient Conditions, *Adv. Mater.* 30 (2018) 1803694.
- [10] S. Chen, S. Perathoner, C. Ampelli, C. Mebrahtu, D. Su, G. Centi, Room-Temperature Electrocatalytic Synthesis of NH_3 from H_2O and N_2 in a Gas–Liquid–Solid Three-Phase Reactor, *ACS Sustainable Chem. Eng.* 5 (2017) 7393-7400.
- [11] L. Han, X. Liu, J. Chen, R. Lin, H. Liu, F. Lü, S. Bak, Z. Liang, S. Zhao, E. Stavitski, Atomically dispersed molybdenum catalysts for efficient ambient nitrogen fixation, *Angew. Chem. Int. Ed.* 131 (2019) 2343-2347.
- [12] N. Cao, Z. Chen, K. Zang, J. Xu, J. Zhong, J. Luo, X. Xu, G. Zheng, Doping strain induced bi- Ti^{3+} pairs for efficient N_2 activation and electrocatalytic fixation, *Nat. Commun.* 10 (2019) 2877.
- [13] W. Li, W. Fang, C. Wu, K.N. Dinh, H. Ren, L. Zhao, C. Liu, Q. Yan, Bimetal–MOF nanosheets as efficient bifunctional electrocatalysts for oxygen evolution and nitrogen reduction reaction, *J. Mater. Chem. A* 8 (2020) 3658-3666.
- [14] Y. Guo, Z. Yao, B.J.J. Timmer, X. Sheng, L. Fan, Y. Li, F. Zhang, L. Sun, Boosting nitrogen reduction reaction by bio-inspired FeMoS containing hybrid electrocatalyst over a wide pH range, *Nano Energy* 62 (2019) 282-288.
- [15] M. Wang, S. Liu, T. Qian, J. Liu, J. Zhou, H. Ji, J. Xiong, J. Zhong, C. Yan, Over 56.55% Faradaic efficiency of ambient ammonia synthesis enabled by positively shifting the reaction potential, *Nat. Commun.* 10 (2019) 341.
- [16] D. Wu, H. Wang, H. Huang, R. Zhang, L. Ji, H. Chen, Y. Luo, J. You, D. Tang, Z. Zhang, Ambient electrochemical N_2 reduction to NH_3 under alkaline conditions enabled by a layered $K_2Ti_4O_9$ nanobelt, *Chem. Commun.* 55 (2019) 7546-7549.
- [17] J. Lv, S. Wu, Z. Tian, Y. Ye, J. Liu, C. Liang, Construction of PdO–Pd interfaces assisted by laser irradiation for

- enhanced electrocatalytic N₂ reduction reaction, *J. Mater. Chem. A* 7 (2019) 12627-12634.
- [18] W. Fu, Y. Cao, Q. Feng, W.R. Smith, P. Dong, M. Ye, J. Shen, Pd-Co nanoalloys nested on CuO nanosheets for efficient electrocatalytic N₂ reduction and room-temperature Suzuki–Miyaura coupling reaction, *Nanoscale* 11 (2019) 1379-1385.
- [19] H.-M. Liu, S.-H. Han, Y. Zhao, Y.-Y. Zhu, X.-L. Tian, J.-H. Zeng, J.-X. Jiang, B.Y. Xia, Y. Chen, Surfactant-free atomically ultrathin rhodium nanosheet nanoassemblies for efficient nitrogen electroreduction, *J. Mater. Chem. A* 6 (2018) 3211-3217.
- [20] W. Xu, F. Lyu, Y. Bai, A. Gao, J. Feng, Z. Cai, Y. Yin, Porous cobalt oxide nanoplates enriched with oxygen vacancies for oxygen evolution reaction, *Nano Energy* 43 (2018) 110-116.
- [21] R. Zhang, Y.-C. Zhang, L. Pan, G.-Q. Shen, N. Mahmood, Y.-H. Ma, Y. Shi, W. Jia, L. Wang, X. Zhang, W. Xu, J.-J. Zou, Engineering Cobalt Defects in Cobalt Oxide for Highly Efficient Electrocatalytic Oxygen Evolution, *ACS Catal.* 8 (2018) 3803-3811.
- [22] L. Zhuang, L. Ge, Y. Yang, M. Li, Y. Jia, X. Yao, Z. Zhu, Ultrathin Iron-Cobalt Oxide Nanosheets with Abundant Oxygen Vacancies for the Oxygen Evolution Reaction, *Adv. Mater.* 29 (2017) 1606793.
- [23] X. Li, J. Wei, Q. Li, S. Zheng, Y. Xu, P. Du, C. Chen, J. Zhao, H. Xue, Q. Xu, H. Pang, Nitrogen-Doped Cobalt Oxide Nanostructures Derived from Cobalt-Alanine Complexes for High-Performance Oxygen Evolution Reactions, *Adv. Funct. Mater.* 28 (2018) 1800886.
- [24] Y. Xu, B. Li, S. Zheng, P. Wu, J. Zhan, H. Xue, Q. Xu, H. Pang, Ultrathin two-dimensional cobalt–organic framework nanosheets for high-performance electrocatalytic oxygen evolution, *J. Mater. Chem. A* 6 (2018) 22070-22076.
- [25] P. Thangasamy, S. Oh, S. Nam, H. Randriamahazaka, I.K. Oh, Ferrocene-Incorporated Cobalt Sulfide Nanoarchitecture for Superior Oxygen Evolution Reaction, *Small* 16 (2020) 2001665.
- [26] M. Yu, F. Waag, C.K. Chan, C. Weidenthaler, S. Barcikowski, H. Tuysuz, Laser Fragmentation-Induced Defect-Rich Cobalt Oxide Nanoparticles for Electrochemical Oxygen Evolution Reaction, *ChemSusChem* 13 (2020) 520-528.
- [27] Y. Ding, J. Zhao, W. Zhang, J. Zhang, X. Chen, F. Yang, X. Zhang, Single-Walled Carbon Nanotubes Wrapped CoFe₂O₄ Nanorods with Enriched Oxygen Vacancies for Efficient Overall Water Splitting, *ACS Appl. Energy Materials* 2 (2018) 1026-1032.
- [28] Y.V. Kaneti, Y. Guo, N.L.W. Septiani, M. Iqbal, X. Jiang, T. Takei, B. Yulianto, Z.A. Allothman, D. Golberg, Y. Yamauchi, Self-templated fabrication of hierarchical hollow manganese-cobalt phosphide yolk-shell spheres for enhanced oxygen evolution reaction, *Chem. Eng. J.* 405 (2021) 126580.
- [29] K. Zhang, G. Zhang, J. Qu, H. Liu, Zinc Substitution-Induced Subtle Lattice Distortion Mediates the Active Center of Cobalt Diselenide Electrocatalysts for Enhanced Oxygen Evolution, *Small* 16 (2020) 1907001.
- [30] X. Hu, S. Zhang, J. Sun, L. Yu, X. Qian, R. Hu, Y. Wang, H. Zhao, J. Zhu, 2D Fe-containing cobalt phosphide/cobalt oxide lateral heterostructure with enhanced activity for oxygen evolution reaction, *Nano Energy* 56 (2019) 109-117.
- [31] Z. Liu, Z. Xiao, G. Luo, R. Chen, C.L. Dong, X. Chen, J. Cen, H. Yang, Y. Wang, D. Su, Y. Li, S. Wang, Defects-Induced In-Plane Heterophase in Cobalt Oxide Nanosheets for Oxygen Evolution Reaction, *Small* 15 (2019) 1904903.
- [32] S. Xu, C. Lv, T. He, Z. Huang, C. Zhang, Amorphous film of cerium doped cobalt oxide as a highly efficient electrocatalyst for oxygen evolution reaction, *J. Mater. Chem. A* 7 (2019) 7526-7532.
- [33] F. Wang, K. Ma, W. Tian, J. Dong, H. Han, H. Wang, K. Deng, H. Yue, Y.X. Zhang, W. Jiang, J. Ji, P-Doped NiMoO₄ parallel arrays anchored on cobalt carbonate hydroxide with oxygen vacancies and mass transfer channels for supercapacitors and oxygen evolution, *J. Mater. Chem. A* 7 (2019) 19589-19596.
- [34] F. Lyu, Y. Bai, Q. Wang, L. Wang, X. Zhang, Y. Yin, Coordination-assisted synthesis of iron-incorporated cobalt oxide nanoplates for enhanced oxygen evolution, *Mater. Today Chem.* 11 (2019) 112-118.
- [35] Y.-N. Hou, Z. Zhao, H. Zhang, C. Zhao, X. Liu, Y. Tang, Z. Gao, X. Wang, J. Qiu, Designed synthesis of cobalt

nanoparticles embedded carbon nanocages as bifunctional electrocatalysts for oxygen evolution and reduction, *Carbon* 144 (2019) 492-499.

[36] C. Du, Y. Gao, J. Wang, W. Chen, Achieving 59% faradaic efficiency of the N_2 electroreduction reaction in an aqueous Zn- N_2 battery by facilely regulating the surface mass transport on metallic copper, *Chem. Commun.* 55 (2019) 12801-12804.

[37] H. Wang, J. Si, T. Zhang, Y. Li, B. Yang, Z. Li, J. Chen, Z. Wen, C. Yuan, L. Lei, Y. Hou, Exfoliated metallic niobium disulfate nanosheets for enhanced electrochemical ammonia synthesis and Zn- N_2 battery, *Appl. Catal. B* 270 (2020) 118892.

[38] X.-W. Lv, Y. Liu, Y.-S. Wang, X.-L. Liu, Z.-Y. Yuan, Encapsulating vanadium nitride nanodots into N,S-codoped graphitized carbon for synergistic electrocatalytic nitrogen reduction and aqueous Zn- N_2 battery, *Appl. Catal. B* 280 (2021) 119434.